Monthly Notices of the ROYAL ASTRONOMICAL SOCIETY
MNRAS **445,** 201–212 (2014) doi:10.1093/mnras/stu1623

Disentangling a group of lensed submm galaxies at $z\sim 2.9$

Todd P. MacKenzie,[1★] Douglas Scott,[1] Ian Smail,[2] Edward L. Chapin,[3] Scott C. Chapman,[4] A. Conley,[5] Asantha Cooray,[6,7] James S. Dunlop,[8] D. Farrah,[9] M. Fich,[10] Andy G. Gibb,[1] Wayne S. Holland,[8,11] R. J. Ivison,[8] Tim Jenness,[12,13] Jean-Paul Kneib,[14] Gaelen Marsden,[1] Johan Richard,[15] E. I. Robson,[8,11] Ivan Valtchanov[16] and Julie L. Wardlow[17]

Affiliations are listed at the end of the paper

Accepted 2014 August 8. Received 2014 July 11; in original form 2013 December 2

ABSTRACT

MS 0451.6−0305 is a rich galaxy cluster whose strong lensing is particularly prominent at submm wavelengths. We combine new Submillimetre Common-User Bolometer Array (SCUBA)-2 data with imaging from *Herschel* Spectral and Photometric Imaging Receiver (SPIRE) and PACS and *Hubble Space Telescope* in order to try to understand the nature of the sources being lensed. In the region of the 'giant submm arc', we uncover seven multiply imaged galaxies (up from the previously known four), of which six are found to be at a redshift of $z \sim 2.9$, and possibly constitute an interacting system. Using a novel forward-modelling approach, we are able to simultaneously deblend and fit spectral energy distributions to the individual galaxies that contribute to the giant submm arc, constraining their dust temperatures, far-infrared luminosities, and star formation rates (SFRs). The submm arc first identified by SCUBA can now be seen to be composed of at least five distinct sources, four of these within a galaxy group at $z \sim 2.9$. Only a handful of lensed galaxy groups at this redshift are expected on the sky, and thus this is a unique opportunity for studying such systems in detail. The total unlensed luminosity for this galaxy group is $(3.1 \pm 0.3) \times 10^{12}\,\mathrm{L}_{\odot}$, which gives an unlensed SFR of $(450 \pm 50)\,\mathrm{M}_{\odot}\,\mathrm{yr}^{-1}$. This finding suggests that submm source multiplicity, due to physically associated groupings as opposed to chance alignment, extends to fainter flux densities than previously discovered. Many of these systems may also host optical companions undetected in the submm, as is the case here.

Key words: gravitational lensing: strong – methods: data analysis – galaxies: clusters: individual – galaxies: interactions – galaxies: starburst – submillimetre: galaxies.

1 INTRODUCTION

Gravitational lensing has been a useful tool for enabling submm studies. The first results from the Submillimetre Common-User Bolometer Array (SCUBA) submm camera on the James Clerk Maxwell Telescope (JCMT; e.g. Smail, Ivison & Blain 1997) used 'nature's telescope' to increase the detection rate of high-redshift submm sources and effectively beat the confusion limit for single-dish studies. Now, *Herschel* (Pilbratt et al. 2010) has found that lensing is significant for some of the brightest submm sources, with surveys such as H-ATLAS and HerMES (*Herschel* Multi-tiered Extragalactic Survey) turning up a population of sources which are boosted enough that they can be studied in great detail in follow-up observations (e.g. Negrello et al. 2010; Wardlow et al. 2013). However, the limited resolution of *Herschel*, and of non-interferometric ground-based observatories such as the JCMT, means that the effects of source blending are a cause of uncertainty in interpreting the results (e.g. Karim et al. 2013), made more difficult in practice, since submm-bright sources are known to be typically merging or interacting systems, where disentangling the contribution to the combined spectral energy distribution (SED) is more complicated still. Even worse – while lensing is nominally achromatic, strong lensing of inhomogeneous extended sources within finite beams is *not* achromatic, since unresolved regions with different spectral properties can be lensed by different amounts. Thus, the existence of strong lensing can be a double-edged sword, boosting the brightness of some sources, but making the detailed interpretation of their SEDs problematic (Serjeant 2012). Multiwavelength studies are key to understanding these complex systems.

MS 0451.6−0305, a massive galaxy cluster at a redshift of 0.55, is lensing several background sources and has been imaged at many

★ E-mail: todd@phas.ubc.ca

© 2014 The Authors
Published by Oxford University Press on behalf of the Royal Astronomical Society

different wavelengths: X-ray (Donahue et al. 2003), optical (Gioia & Luppino 1994; Takata et al. 2003; Kodama et al. 2005; Moran et al. 2007; Zitrin et al. 2011), near-infrared (IR; Borys et al. 2004; Wardlow et al. 2010), mid-IR (Geach et al. 2006), far-infrared (far-IR; Oliver et al. 2012), mm/submm (Chapman et al. 2002a; Borys et al. 2004; Wardlow et al. 2010), and radio (Reese et al. 2000; Berciano Alba et al. 2010). In the optical, the previously discovered multiply imaged sources include an extended optical arc composed of a Lyman-break galaxy (LBG) with a spectroscopic redshift of $z = 2.911$, as well as two extremely red objects (EROs) with a redshift of $z = 2.9 \pm 0.1$, determined from lensing models (Borys et al. 2004; Berciano Alba et al. 2010). The two EROs and the LBG are so close in separation (∼10 kpc in projection) that they potentially constitute an interacting system. A fourth multiply imaged galaxy was discovered by Zitrin et al. (2011).

The steep number counts in the submm make lensing much more striking in this waveband than the optical – at 850 μm, the SCUBA map of the cluster core showed a 'giant submm arc', by far the brightest feature in this region of the sky, with an extent of around 1 arcmin, consistent with the blending of multiple galaxy images which lie near the critical line in the lensing model. If the optical galaxies are indeed interacting, the submm arc could be attributed to triggered star formation within one or more of these galaxies. This scenario is also supported by the radio data, as discussed in Berciano Alba et al. (2010).

New observations, presented here using the Wide Field Camera 3 (WFC3) on *Hubble Space Telescope* (*HST*), SCUBA-2 on the JCMT, and PACS and Spectral and Photometric Imaging Receiver (SPIRE) on *Herschel*,[1] shed new light on what is generating the submm arc. With the deeper *HST* images, and a new LENSTOOL (Kneib et al. 1996; Jullo et al. 2007; Jullo & Kneib 2009) lensing model, there are now *seven* known multiply imaged galaxies (including the previously known four) in the region of the submm arc. Six of these multiply imaged galaxies are consistent with a redshift of $z \sim 2.9$ and probably constitute an interacting galaxy group. To properly analyse the submm imaging of SCUBA-2 and *Herschel*, we have developed a new approach to disentangle the confused components generating the submm arc, which fully exploits the multiply imaged and differentially magnified nature of the system, and allows us to directly estimate both the dust temperature, $T_{\rm d}$, and the far-IR luminosity, $L_{\rm IR}$ (and thus star formation rate, SFR), for each of the contributing galaxies. This allows us to investigate the $T_{\rm d}$ versus $L_{\rm IR}$ relation for intrinsically less luminous galaxies at high-z than traditional blank field surveys. Possible evolution of this relation with redshift allows us to probe the properties of star formation in the early Universe (e.g. Chapman et al. 2002b, 2005; Kovács et al. 2006; Pope et al. 2006; Chapin et al. 2011; Symeonidis et al. 2013; Sklias et al. 2014; Smail et al. 2014; Swinbank et al. 2014). Our method significantly improves upon the conventional method of extracting sources, or smoothing and binning multiwavelength data to the worst resolution, before fitting SEDs (a process that destroys useful information).

This paper is organized as follows. In Section 2, we introduce the *HST* optical data and the lensing model. In Section 3.1, we present the SCUBA-2 data and in Section 3.2 the *Herschel* data. In Section 4.1, we present the SED model and image reconstruction methods and in Section 4.2 the model fitting procedure. Section 5.1 discusses the results and Section 6 finishes with the conclusions. Throughout we employ a Λ cold dark matter (ΛCDM) cosmology with $\Omega_\Lambda = 0.7$, $\Omega_{\rm m} = 0.3$, and $H_0 = 70\,{\rm km\,s^{-1}\,Mpc^{-1}}$.

[1] *Herschel* is an ESA space observatory with science instruments provided by European-led Principal Investigator consortia and with important participation from NASA.

2 *HST* AND THE LENSING MODEL

Although the main motivation for our study comes from the new submm data, it makes the most scientific sense to first describe the optical data. We retrieved previously unpublished observations using WFC3 on *HST* from the Canadian Astronomical Data Centre (programme 11591). The observations were taken at 1.1 and 1.6 μm with 2400 and 2600 s exposures, respectively. A small pointing shift in the data, with respect to *HST* data published by Borys et al. (2004) and Berciano Alba et al. (2010), was corrected by aligning to the older *HST* data in this field. These observations reveal a host of new red objects in the region of the submm arc (Fig. 1).

Using LENSTOOL (Kneib et al. 1996; Jullo et al. 2007; Jullo & Kneib 2009) and a new lensing model for the cluster, we were able to identify *three* new multiply imaged galaxies within the *HST* images in the region of the submm arc. Table 1 lists the positions, amplifications factors, and redshift estimates derived from our model for each of the seven multiply imaged galaxies within the region of the submm arc. Fig. 1 shows the close positional arrangement of the multiple images with respect to the 'giant submm arc' and the available submm data. Enlarged cut-outs of the multiply imaged galaxies are shown in Fig. 2. Borys et al. (2004) have already suggested that Galaxies 5, 6, and 7 are likely to be an interacting group at $z \sim 2.9$. Our new model supports their analysis and adds Galaxies 2, 3, and 4 to the same group, expanding it to a group of six galaxies at $z \sim 2.9$. Galaxy 1 is found to have a slightly higher redshift of $z = 3.11 \pm 0.03$ derived from the lensing model, and thus is not likely associated with the interacting group.

Galaxy 8 is not multiply imaged, but has similar colours to the rest of the multiply imaged galaxies and has a disturbed morphology. If it is at the same redshift as the interacting group, our lensing model predicts no multiple images, consistent with the observations but yielding no additional constraints on its redshift from the lensing model. However, we have found that submm emission originating from near its position is important for reproducing the morphology of the submm arc (see Section 5.1), and thus we have included it in our model (see Section 4).

Galaxy 9 is a foreground galaxy at $z = 0.157$ and has associated Multiband Imaging Photometer (MIPS) 24 μm (not described here) and PACS emission (see Section 3.2); thus, it is also included in our model as a possible source of submm emission.

It is apparent that the nature of the submm arc is significantly more complicated than previously thought and is likely a combination of several of the galaxies described above. More details concerning the LENSTOOL modelling will be presented in a forthcoming paper by Swinbank et al. (2014).

3 NEW SUBMM IMAGING

3.1 SCUBA-2

The cluster was observed with SCUBA-2 (Holland et al. 2013) on the JCMT during commissioning, as part of 'Guaranteed Time' for the instrument team. A total of 12.7 h between 2010 February and 2012 February achieved an rms of 15 mJy beam^{-1} at 450 μm using 2 arcsec pixels and 1.2 mJy beam^{-1} at 850 μm using 4 arcsec pixels. Since the submm arc had already been observed at 850 μm using SCUBA (Borys et al. 2004), the motivations for the

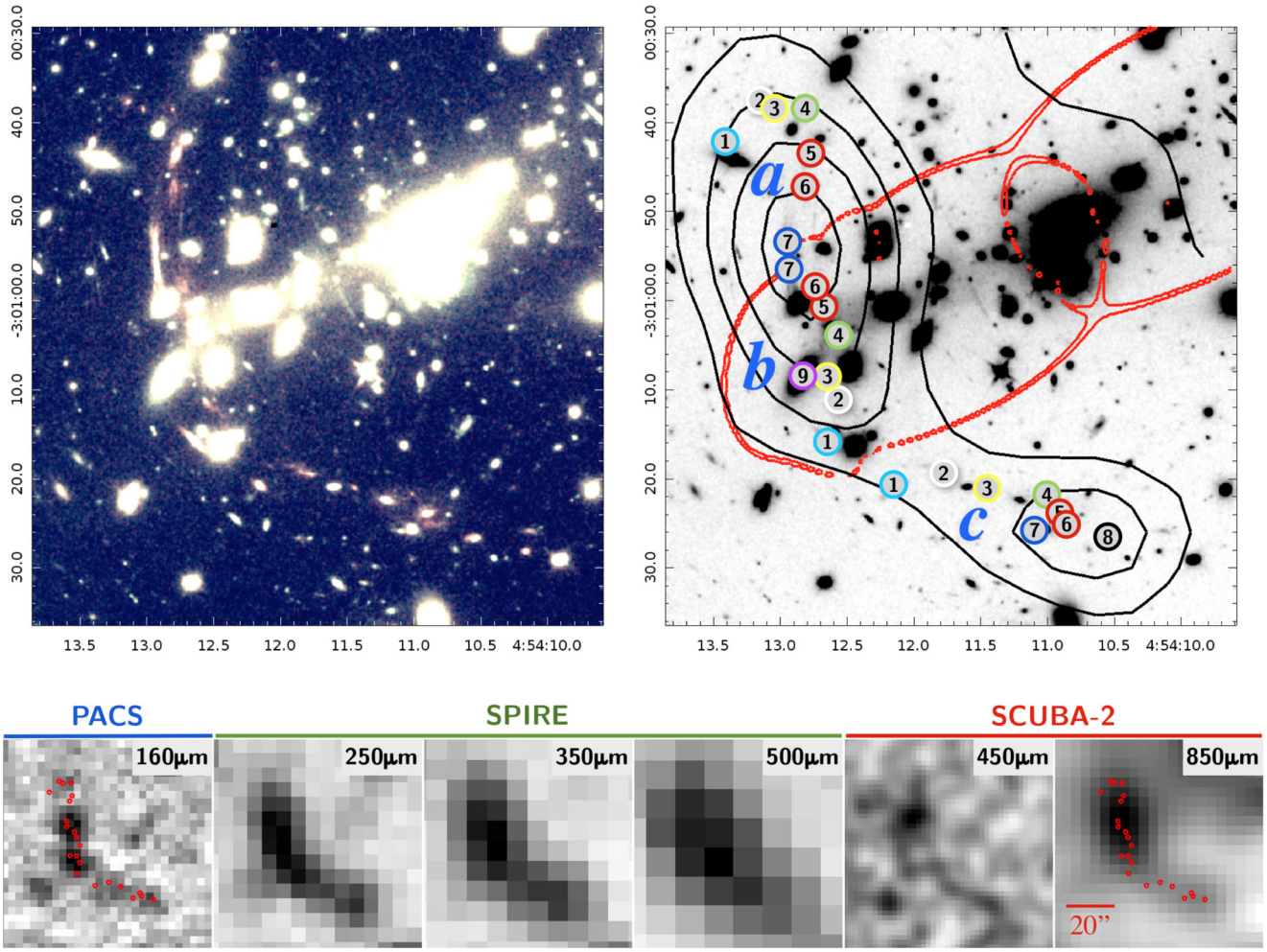

Figure 1. Top-left panel: *HST* WFC3 colour composite (red: 1.6 μm, green: 1.6 + 1.1 μm, blue: 1.1 μm), clearly showing the main optical arc (roughly vertical, at about RA = $4^{h}54^{m}12^{s}.9$), offset slightly from the abundance of red images along the submm arc. The contrast has been stretched to highlight the faint arcs and multiply imaged galaxies. Top-right panel: *HST* image (1.6 + 1.1 μm) with the positions of the multiply imaged galaxies labelled numerically from 1 through 7, with sub-groups of images labelled as *a, b,* and *c*. The galaxy discovered by Zitrin et al. (2011) is labelled as Galaxy 1 and the two EROs and the LBG discovered by Borys et al. (2004) are labelled Galaxy 5, 6, and 7, respectively. The red contour denotes the critical line of the lensing model for a redshift of $z = 2.911$, while the black contours represent the SCUBA-2 850 μm emission. Galaxy 8 is a singly imaged source with colours similar to those of the other multiply imaged galaxies, and has been found to be important when trying to reproduce the morphology of the submm arc. Galaxy 9 is a foreground galaxy at a redshift of $z = 0.157$. Bottom: the ‘giant submm arc’ as seen by *Herschel* PACS and SPIRE and SCUBA-2 over more than a factor of 5 in wavelength range. The red circles plotted on the shortest and longest wavelength images mark the positions of the galaxies depicted in the top-right panel. It is obvious that this string of multiply imaged $z \sim 2.9$ galaxy group sources are responsible for generating the majority of the submm arc. However, they are too spatially confused for traditional deblending techniques.

new observations were (1) to confirm the bright lensed structure with SCUBA-2, without the complications introduced by SCUBA’s requirement to chop (Borys et al. 2004), and (2) to detect the lensed structure at 450 μm, at a resolution better by about a factor of 2, with the hope of resolving the submm arc into individual sources. The data were reduced using a configuration file optimized for blank fields using the SMURF data reduction software for SCUBA-2 (Chapin et al. 2013).

At 850 μm, the submm arc is detected at high signal-to-noise by SCUBA-2 (see Fig. 1). Its brightest part is elongated roughly north–south, and at the southern end curves to the west, just as in the original SCUBA image. The higher resolution 450 μm data trace a largely similar structure, but at a lower relative sensitivity, with a signal-to-noise ratio of about 3 after smoothing with the beam, for the brightest portion of the lensed emission. The SCUBA-2 data are constrained by both resolution at 850 μm and sensitivity at 450 μm, and thus only limited conclusions can be obtained from these two channels alone. Fig. 1 shows the SCUBA-2 data alongside the *Herschel* SPIRE and PACS images for comparison, and also it shows smoothed 850 μm contours plotted over the *HST* imaging.

3.2 *Herschel*

Confusion-limited images of MS 0451.6−0305 using *Herschel* SPIRE (Griffin et al. 2010; Swinyard et al. 2010) were taken as part of the guaranteed time programme HerMES (Oliver et al. 2012). The cluster was imaged at the three SPIRE wavelengths of 250, 350, and 500 μm with full width at half-maximum (FWHM) beam sizes of 18.1, 24.9, and 36.2 arcsec, respectively (Griffin et al. 2010). A total of 18.3 h of observation reached an rms of 1.5, 1.5, and

Table 1. List of images for the eight high-z galaxies, as well as one low-redshift interloper at $z = 0.157$. The galaxy IDs denote each galaxy, as shown in Fig. 1, and the letters indicate the multiple images of each galaxy (with *a* being the most northern images in each case and *c* being the most southern images). The position of image 4.b, as inferred from the lensing model, is obscured by foreground cluster galaxies. The amplification factors are derived from the LENSTOOL modelling in Section 2. The redshift of Galaxy 8 is unknown, but has similar colours to the other high-redshift multiply imaged galaxies, a disturbed morphology, and was found to be important for reproducing the SW extension of the submm arc; thus, we assume a nominal redshift of 2.9. The superscript letters on the redshifts denote the method by which they were derived: *a* for redshifts derived from the lensing model, *b* for a spectroscopic redshift, and *c* for a nominally chosen value. The reported magnitudes are AB magnitudes.

Gal ID	RA J2000	Dec. J2000	$F160W$	$F110W$	Amplification	Redshift	Notes
1.a	04:54:13.42	−3:00:43.0	21.94 ± 0.01	23.26 ± 0.01	3.80 ± 0.06	3.11 ± 0.03^a	(Takata et al. 2003; Zitrin et al. 2011)
1.b	04:54:12.65	−3:01:16.5	20.91 ± 0.01	22.27 ± 0.01	20 ± 1		(Takata et al. 2003; Zitrin et al. 2011)
1.c	04:54:12.17	−3:01:21.4	21.86 ± 0.01	23.18 ± 0.01	7.3 ± 0.1		(Takata et al. 2003; Zitrin et al. 2011)
2.a	04:54:13.15	−3:00:38.4	24.15 ± 0.03	24.74 ± 0.05	2.86 ± 0.04	2.91 ± 0.04^a	
2.b	04:54:12.58	−3:01:11.9	23.62 ± 0.03	24.25 ± 0.05	8.1 ± 0.4		
2.c	04:54:11.79	−3:01:20.2	22.88 ± 0.02	23.85 ± 0.04	6.1 ± 0.1		
3.a	04:54:13.04	−3:00:39.2	24.98 ± 0.04	26.28 ± 0.07	3.19 ± 0.05	2.94 ± 0.04^a	
3.b	04:54:12.68	−3:01:09.1	23.27 ± 0.02	24.09 ± 0.05	2.98 ± 0.05		
3.c	04:54:11.46	−3:01:21.7	24.27 ± 0.04	25.49 ± 0.06	4.31 ± 0.08		
4.a	04:54:12.82	−3:00:39.3	24.82 ± 0.05	26.39 ± 0.08	3.57 ± 0.06	2.94 ± 0.04^a	
4.b	04:54:12.53	−3:01:04.5	26.64 ± 0.07	27.50 ± 0.09	6.2 ± 0.2		Lensing model position
4.c	04:54:11.03	−3:01:22.4	24.70 ± 0.05	25.90 ± 0.07	3.36 ± 0.06		
5.a	04:54:12.81	−3:00:44.4	21.73 ± 0.01	23.51 ± 0.01	5.3 ± 0.1	2.89 ± 0.03^a	ERO-B (Borys et al. 2004)
5.b	04:54:12.69	−3:01:01.5	21.81 ± 0.01	23.47 ± 0.01	6.4 ± 0.1		ERO-B (Borys et al. 2004)
5.c	04:54:10.93	−3:01:24.6	21.97 ± 0.01	23.78 ± 0.02	2.89 ± 0.04		ERO-B (Borys et al. 2004)
6.a	04:54:12.81	−3:00:47.5	22.62 ± 0.02	24.55 ± 0.06	8.2 ± 0.2	2.86 ± 0.03^a	ERO-C (Borys et al. 2004)
6.b	04:54:12.72	−3:00:59.6	24.41 ± 0.04	26.60 ± 0.15	4.98 ± 0.08		ERO-C (Borys et al. 2004)
6.c	04:54:10.88	−3:01:25.8	22.85 ± 0.02	24.67 ± 0.09	2.76 ± 0.04		ERO-C (Borys et al. 2004)
7.a	04:54:12.95	−3:00:54.8	21.80 ± 0.01	22.26 ± 0.01	33 ± 2	2.911 ± 0.003^b	LBG (Borys et al. 2004)
7.b	04:54:12.93	−3:00:57.5	22.29 ± 0.01	22.76 ± 0.01	45 ± 3		LBG (Borys et al. 2004)
7.c	04:54:11.11	−3:01:26.6	23.66 ± 0.02	24.23 ± 0.03	2.87 ± 0.04		LBG (Borys et al. 2004)
8	04:54:10.55	−3:01:27.3	22.77 ± 0.02	23.50 ± 0.03	1.73 ± 0.04	2.9^c	Singly imaged
9	04:54:12.85	−3:01:09.1	18.91 ± 0.01	19.19 ± 0.02	–	0.15719^b	Foreground galaxy

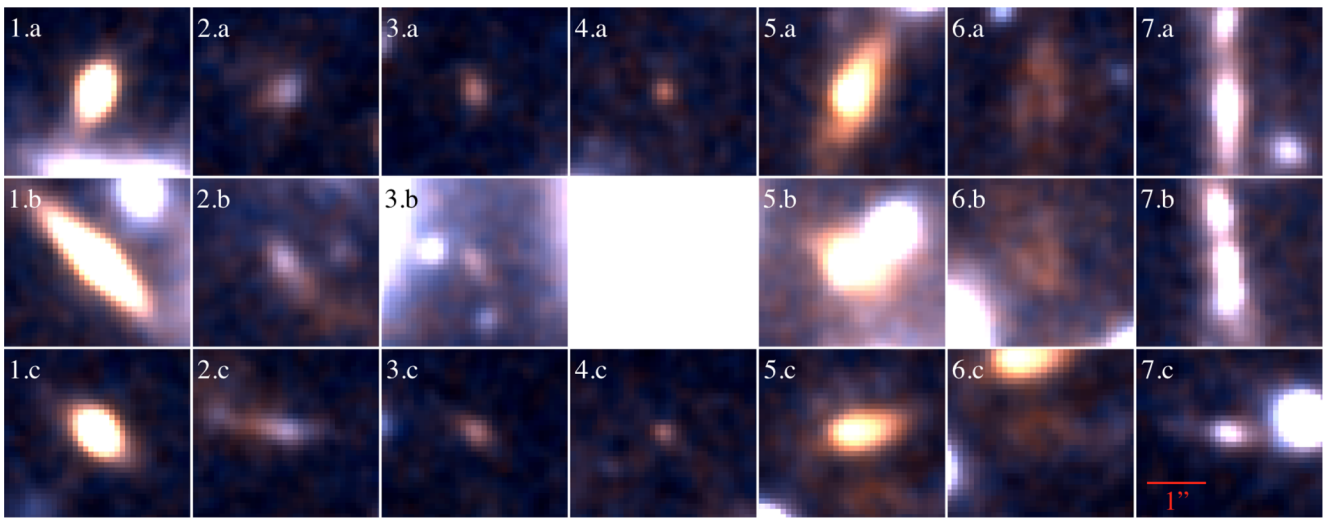

Figure 2. *HST* cut-outs at the locations of the seven multiply imaged galaxies listed in Table 1 with each column displaying the multiple images of a single galaxy. The letters refer to the three sub-groups of images labelled in Fig. 1. Image 4.b is not shown because it is obscured by foreground galaxies. We show a scale bar for all panels in the lower right.

1.7 mJy beam^{-1} at 250, 350, and 500 μm, respectively, with pixel sizes of 6, 8.3, 12 arcsec. A detailed description of the map-making procedure is given in Levenson et al. (2010), and the most recent updated method described in Viero et al. (2013). To ensure accurate astrometry, we have stacked on the positions of over 900 *Spitzer* MIPS 24 μm sources that overlap with the field and have corrected a 1.3 arcsec shift in RA and 0.4 arcsec shift in Dec. The uncertainty in this correction is 0.2 arcsec, calculated by bootstrapping the 24 μm source list.

Two PACS (Poglitsch et al. 2010) observations taken as part of the PACS Evolutionary Probe key programme (Lutz et al. 2011) are also available and were processed using the ‘multiple obsid scanMapDeepSurvey’ pipeline within HIPE 10 (Ott 2010). The default units were converted from Jy pixel^{-1} to Jy beam^{-1} by multiplying

by the beam area and dividing by the pixel area. The beam area for the 160 μm point spread function (PSF) was found to be 180 arcsec,[2] and was computed by integrating over the beam profile provided by the NASA *Herschel* Science Center. A total of 5.2 h of observation reached an rms of 2 mJy beam^{-1} using 3 arcsec pixels. The FWHM at 160 μm is 11.6 arcsec. For galaxies at $z \sim 3$, 70 μm PACS data are expected to be dominated by warm dust, which is not well reproduced by the simple SED model adopted in Section 4, and are therefore not used in this study.

The submm arc is detected across all the available submm bands (see Fig. 1), but with the large number of multiply imaged galaxies (seen in Fig. 1) that are strung along the submm arc, it is unclear which galaxies are contributing. The morphology of the submm arc seen in each image is a function of both the telescope PSFs and the SEDs of the contributing galaxies. In addition to determining which galaxies are contributing, we would also like to constrain their physical properties. With the lensing model well constrained by the *HST* observations (see Section 2) and this wealth of multiwavelength data, it is clear that a comprehensive modelling approach is required.

4 A FRAMEWORK FOR FITTING SEDS TO CONFUSED COUNTERPARTS

Both Borys et al. (2004) and Berciano Alba et al. (2010) performed limited modelling of the optical and radio counterparts, respectively, in an attempt to reproduce the observed submm arc. Their approach of smoothing different plausible components with the SCUBA 850 μm beam showed that the LBG and two EROs are likely contributors, but neither could fully reproduce the observed submm arc. With new SCUBA-2 and *Herschel* observations, we are able to expand on this approach and have developed a framework for fitting SEDs to the confused optical counterparts, fully exploiting the strong gravitational lensing of this system.

While source plane reconstruction of multiply imaged galaxies is an effective approach for high-resolution imaging (e.g. Kochanek & Narayan 1992; Colley, Tyson & Turner 1996), it fails in the confused regime. Because the galaxies blend together in the submm, it is impractical to trace photons back through the lensing potential and into the source plane, since much of the photon positional information has been lost due to the large telescope beams. Instead, we use the high-resolution *HST* imaging to identify candidate counterparts to the submm galaxies (SMGs) in the optical, and use their positions as priors for the origin of any submm emission. We then forward-model the galaxy SEDs through the telescope filters, and use the amplification factors derived from the lensing model for each galaxy image, to reproduce the submm arc in each wavelength channel separately. Essentially, we are fitting SEDs of galaxies directly to the data, without the need for first deblending and extracting sources or smoothing and re-binning our data to the worst resolution (a process that destroys useful information).

Our method is complementary to that employed by Fu et al. (2012), where they forward-model a single submm source through the gravitational lens, allowing the position to vary, to reproduce the observed morphology of their Submillimeter Array (SMA) and Very Large Array observations. With their model, they were able to show that the source of the gas and dust emission was offset from the optical counterpart. However, the gravitational lensing in this case is galaxy–galaxy lensing and the observations have much higher resolution than either the SCUBA-2 or *Herschel* observations presented here. The gravitational lensing presented here is for a group of galaxies being lensed by a foreground cluster and thus the set of multiple images subtends a much larger area on the sky than galaxy–galaxy lensing. The optical imaging provides positions which are more than adequate for our purposes, since, with the resolutions of SCUBA-2 and *Herschel*, any small offset of the submm emission from their optical counterparts will not have a strong effect on the morphology of the submm arc; the strongest effect of an offset would be seen in the relative amplifications of the multiple images. Our method is novel in that we reproduce the morphology of the submm emission across multiple wavelengths, while simultaneously fitting source SEDs, thus tying together the multiwavelength data. These two complementary techniques (detailed source plane reconstruction and forward-modelling SEDs at fixed source positions) could be combined in the future, given the proper observations.

4.1 Model SED and image reconstruction

The first ingredient we need is an SED model for our galaxies in the submm. For the longer wavelength channels of SCUBA-2 and *Herschel* SPIRE, the SED of a galaxy is well represented by a modified blackbody with a single temperature:

$$S(\nu, T_{\mathrm{d},i}, z_i, C_i) = C_i \left(\frac{\nu(1+z_i)}{\nu_0}\right)^{\beta} (\nu(1+z_i))^3 \left[\exp\left(\frac{h\nu(1+z_i)}{k_{\mathrm{B}} T_{\mathrm{d},i}}\right) - 1\right]^{-1}, \quad (1)$$

where S is the flux density, ν is the observed frequency, $\nu_0 = 1.2\,\mathrm{THz} = c/(250\,\mu\mathrm{m})$, β is the dust emissivity, $T_{\mathrm{d},i}$ is the dust temperature, z_i is the redshift, C_i is a normalization factor, and the subscript i denotes the galaxy. We have virtually no constraining power on the dust emissivity, primarily due to the confused nature of the data, and we therefore fix it to a nominal value of 1.5. Due to the high redshifts of our galaxies, the shorter wavelength channels of *Herschel* are dominated by hot dust and are better represented by a power law on the Wien side, i.e.

$$S(\nu, T_{\mathrm{d},i}, z_i, C_i) \propto \nu^{-\alpha}, \quad (2)$$

where the power-law amplitude and the frequency at which to switch between the power law and modified blackbody are chosen so that the transition is smooth (i.e. the two functions and their first derivative are continuous); such a model has been used by Pascale et al. (2009), for example. For the same reason that we fix the value of the dust emissivity, we fix α to a nominal value of 2.0 as found by Casey (2012). We then propagate the individual galaxy SEDs through each telescope bandpass filter:

$$\bar{S}_b(T_{\mathrm{d},i}, z_i, C_i) = \frac{\int S(\nu, T_{\mathrm{d},i}, z_i, C_i) T_b(\nu) \mathrm{d}\nu}{\int T_b(\nu) f_b(\nu) \mathrm{d}\nu}, \quad (3)$$

where $\bar{S}_b$ is the galaxy flux density averaged over channel b, $T_b(\nu)$ is the transmission for channel b, and $f_b(\nu)$ is a calibration parameter. For *Herschel*, $f_b(\nu) = \nu_0/\nu$, due to assuming a power-law SED shape for observed sources, where ν_0 is equal to $c/(160\,\mu\mathrm{m})$, $c/(250\,\mu\mathrm{m})$, $c/(350\,\mu\mathrm{m})$, and $c/(500\,\mu\mathrm{m})$ for 160, 250, 350, and 500 μm, respectively. We assume a constant calibration factor, $f_b(\nu) = 1$, for SCUBA-2, since the bandpass filters are relatively narrow and we are firmly on the Rayleigh–Jeans side of the spectrum.

Using the lensing model, the SCUBA-2 and *Herschel* images are reconstructed as follows:

$$M_b(\boldsymbol{x}) = \sum_i \sum_j A_{ij} \bar{S}_b(T_{\mathrm{d},i}, z_i, C_i) P_\nu(\boldsymbol{x} - \boldsymbol{r}_{ij}) + B_b. \quad (4)$$

Here $M_b(\boldsymbol{x})$ is the flux at position $\boldsymbol{x}$ for frequency channel b, A_{ij} is the amplification factor for image j of Galaxy i derived from the lensing model, $P_\nu(\boldsymbol{x} - \boldsymbol{r}_{ij})$ is the response function (i.e. the telescope beam), with $\boldsymbol{r}_{ij}$ denoting the position of image j of Galaxy i, and B_b is the image background.

The response functions for the *Herschel* SPIRE channels are approximated as Gaussians with FWHM of 18.1, 24.9, and 36.2 arcsec at 250, 350, and 500 μm, respectively, and 11.6 arcsec at 160 μm for *Herschel* PACS. Due to the high-pass filtering of the SCUBA-2 data, we need to ensure that we have an accurate model of the effective response function; thus, we simulate 7 and 15 arcsec FWHM point sources, for the 450 and 850 μm data, respectively, within the SMURF data reduction software, and approximate the effective response function by fitting double Gaussians to their resulting shapes. The result for the 450 μm response function is a Gaussian with FWHM of 6.86 arcsec and an amplitude of 0.893, plus a second Gaussian with FWHM of 34.6 arcsec and amplitude of −0.015. The result for the 850 μm response function is a Gaussian with FWHM of 13.9 arcsec and amplitude of 0.869, plus a second Gaussian with FWHM of 25.9 arcsec and amplitude of −0.077.

4.2 Model fitting

The SED model adopted is non-linear and due to the confused nature of this system, we expect there to be some degeneracies between fit parameters. To obtain uncertainties for each fit parameter, determine the degeneracies between them, and efficiently explore the large parameter space required, the model is fitted to the data using an Markov Chain Monte Carlo (MCMC) Metropolis–Hastings algorithm (Metropolis et al. 1953; Hastings 1970) with Gibbs sampling (Geman & Geman 1993). This method has become widely used in astronomy, especially for fitting cosmological parameters (Lewis & Bridle 2002). The method requires a likelihood function to be defined to which the model is fitted. Since the SCUBA-2 450 and 850 μm and PACS 160 μm data are limited by instrumental noise, the log -likelihood functions for these data are calculated as follows:

$$-\log L_b = X_b + \sum_k \frac{(D_b(\boldsymbol{x}_k) - M_b(\boldsymbol{x}_k)/c_b)^2}{2\sigma_{b,k}^2}, \tag{5}$$

where subscript b denotes the band, $D_b(\boldsymbol{x}_k)$ are the data, $\boldsymbol{x}_k$ denotes the position of pixel k in the image, $\sigma_{b,k}^2$ is the instrumental noise for pixel k, c_b is the instrument calibration factor (with a mean value of unity), and X_b is a constant.

The log -likelihood function for the *Herschel* SPIRE data is more complicated, since we are limited by extragalactic confusion noise as opposed to instrumental noise. The confusion limit in each channel is 5.8, 6.3, and 6.8 mJy at 250, 350, and 500 μm, respectively (Nguyen et al. 2010). This means that the residuals after subtracting the model will be (i) much larger than instrumental noise, (ii) correlated spatially with the beam, and (iii) correlated across wavelengths. This is because confusion noise is real signal generated from many faint sources that are all blending together to produce an unknown and correlated variable background. Taking confusion into account, the log -likelihood function for the *Herschel* SPIRE data is therefore

$$-\log L_{\rm SPIRE} = X_{\rm SPIRE} + \frac{1}{2}\mathbf{R}^{\rm T}\mathbf{C}^{-1}\mathbf{R}, \tag{6}$$

where $\mathbf{R}$ is a one-dimensional list of the residuals, and contains all three channels of SPIRE data ($\mathbf{R} = \{D_{250}(\boldsymbol{x}_k) - M_{250}(\boldsymbol{x}_k)/c_{250}, D_{350}(\boldsymbol{x}_k) - M_{350}(\boldsymbol{x}_k)/c_{350}, D_{500}(\boldsymbol{x}_k) - M_{500}(\boldsymbol{x}_k)/c_{500}\}$), and $\mathbf{C}^{-1}$ is the inverse covariance matrix for the residuals. The covariance matrix, $\mathbf{C}$, is estimated using the Great Observatories Origins Deep Survey (GOODS)-North HerMES field, also observed with *Herschel* SPIRE. This is the largest blank *Herschel* field with instrumental noise similar to that of the MS 0451.6−0305 data, and has an area of 0.1 deg^2. To estimate the covariance matrix, we extract cut-outs from the GOODS-North field, with the same dimensions as the MS 0451.6−0305 data, and calculate the covariance between all the pixels. We then average the covariance matrices of each set of cut-outs to obtain an estimate of the true covariance matrix, ignoring regions with standard deviations greater than twice the confusion limit in any channel to avoid regions with significantly bright sources. The total log -likelihood is then

$$\log L_{\rm total} = \log L_{850} + \log L_{450} + \log L_{\rm SPIRE} + \log L_{160}. \tag{7}$$

Flux calibration uncertainties, c_b, are taken into account during the fitting procedure by setting priors on c_b for each band. The flux calibrations of the 160, 450, and 850 μm data are 5, 2.5, and 5 per cent, respectively (Muller et al. 2011; Dempsey et al. 2013). SPIRE waveband calibrations are correlated, with a covariance matrix

$$C = \begin{vmatrix} 0.001\,825 & 0.0016 & 0.0016 \\ 0.0016 & 0.001\,825 & 0.0016 \\ 0.0016 & 0.0016 & 0.001\,825 \end{vmatrix}, \tag{8}$$

where the calibration is normalized to unity (Bendo et al. 2013, 4 per cent correlated uncertainty between bands plus 1.5 per cent uncorrelated between bands). The calibration uncertainties are a small effect when compared to the instrumental and confusion noise within the observations.

We set no prior on the amplitude of the modified blackbodies or each unknown image background. A hard prior, $T > 10$ K, is motivated by the fact that neither Dale et al. (2012) nor Amblard et al. (2010) found any colder *Herschel* galaxies in either the nearby or distant Universe, respectively. While we have corrected the relative pointing of *Herschel* and *HST*, we are unable to find any significant pointing shift in the JCMT due to the lower signal-to-noise in the map than what is available in the *Herschel* SPIRE observations. The nominal pointing accuracy is 1.5 arcsec, and thus we include this as a prior and marginalize over any possible pointing offset along with the image backgrounds.

Table 1 lists the possible contributing galaxies in our model. This consists of the seven multiply imaged galaxies, one singly imaged red galaxy (Galaxy 8) with disturbed morphology, and one foreground galaxy (Galaxy 9) with associated MIPS 24 μm and PACS 160 μm emission. This brings the total to nine possible contributing galaxies. Their positions are derived from the *HST* data and their amplification factors are derived from the lensing model. The redshift of Galaxy 8 is set to a nominal value of $z = 2.9$ and we report the lensed far-IR luminosity and SFR for this galaxy. Galaxy image positions, amplification factors, and redshifts are held fixed during the fitting procedure since their uncertainties are small.

By assuming that the UV radiation of hot young stars is completely absorbed and re-radiated at longer wavelengths by intervening dust, as well as assuming an initial mass function and a starburst model, it is possible to estimate a rough conversion factor between bolometric luminosity and SFR (e.g. Lehnert & Heckman 1996; Meurer et al. 1997; Kennicutt 1998). Here, we convert far-IR luminosities, calculated by integrating the rest-frame SEDs from 8 to

1000 μm, to SFRs using the relation estimated by Murphy et al. (2011):

$$\mathrm{SFR} = 1.49 \times 10^{-10}\,\mathrm{M}_{\odot}\,\mathrm{yr}^{-1} L_{\mathrm{FIR}}/\mathrm{L}_{\odot}. \quad (9)$$

When reporting the uncertainties in our SFR values for each galaxy in our model, we consider only the uncertainty in far-IR luminosity and do not include any uncertainty in this relation.

5 RESULTS AND DISCUSSION

5.1 A compact group of galaxies at high redshift

All galaxies listed in Table 1 are included in our model and when fitted, we can clearly identify Galaxies 2, 6, 7, 8, and 9 as the sources of submm emission generating the submm arc. Fig. 3 shows the positional arrangement of the $z \sim 2.9$ galaxy group in the source plane with squares highlighting the galaxies responsible for generating the majority of the submm arc. Fig. 5 shows the data, the best-fitting model, and the residuals after subtracting the model from the data. Also included in the figure is a decomposition of the submm arc into the unique contributions of each galaxy to the total best-fitting model. Fig. 6 shows the MCMC likelihood contours for temperature and far-IR luminosity for these five galaxies, and Table 2 lists the results along with SFRs and upper limits for Galaxies 1, 3, 4, and 5. It is apparent in the MCMC likelihood contours that there is a strong degeneracy between the far-IR luminosities of Galaxies 6 and 7.

Fig. 6 shows a degeneracy between the luminosity of Galaxy 6 versus Galaxy 5 in our model, due to their close proximity. While our model prefers emission from Galaxy 6, Berciano Alba et al. (2010) found that Galaxy 5 has associated radio emission, and hence we might consider that the submm emission attributed to Galaxy 6 in our model actually originates from Galaxy 5. We can test this hypothesis using the far-IR-to-radio correlation to predict a luminosity for Galaxy 5 and by also removing Galaxy 6 from our model and performing the fitting procedure again (thus, forcing our model to attribute a portion of its luminosity to Galaxy 5), and then comparing the results. When doing so, we find that Galaxy 5 is attributed a luminosity of $(4.5 \pm 0.9) \times 10^{11}\,\mathrm{L}_{\odot}$ by our model (i.e. essentially all the luminosity of Galaxies 5 and 6 together). Using the peak flux

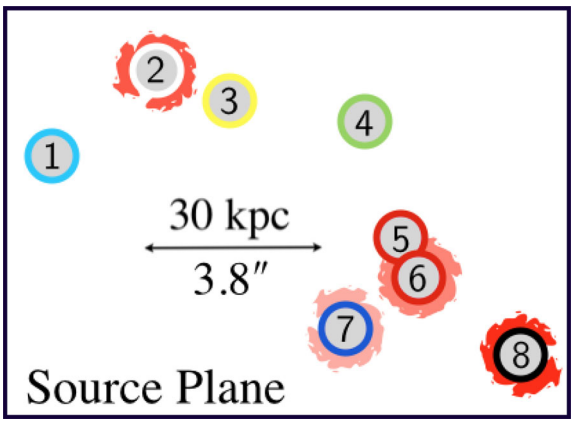

Figure 3. Source plane arrangement of the $z \sim 2.9$ group galaxies. Galaxies 2 through 7 are consistent with being at this redshift. Galaxy 1 lies at a slightly higher redshift, while Galaxy 8 is assumed to be part of the $z \sim 2.9$ group. The galaxies found to be generating the majority of the submm arc are highlighted with red backgrounds and scale with their measured far-IR luminosity. The galaxies are spread over no more than ∼100 kpc in projection, with many components separated by ∼ 10–20 kpc.

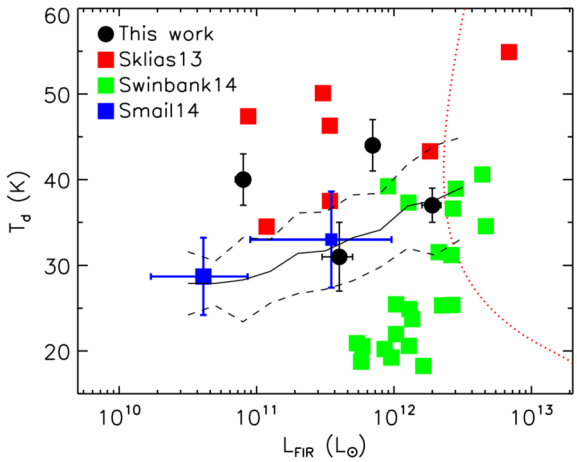

Figure 4. Dust temperature versus far-IR luminosity for several samples of galaxies. The solid line shows the trend found by Symeonidis et al. (2013) using *Herschel* for $z \sim 0$–1.5 galaxies, with the dashed lines showing the dispersion of the sample. The green squares are the LESS SMGs followed up by Swinbank et al. (2014) with ALMA and *Herschel*, with $z \sim 1$–6. The blue squares are the results of stacking on narrow-band [O II] emitters (left) and MIPS+radio sources not detected in SPIRE/SCUBA-2 (right) for a $z = 1.6$ cluster (Smail et al. 2014). The red squares are a sample of lensed SMGs discovered with *Herschel* (Sklias et al. 2014) with $z \sim 1.5$–3. The black circles are the four $z \sim 2.9$ group galaxies that compose the submm arc of MS 0451.6−0305. Both Swinbank et al. (2014) and Symeonidis et al. (2013) found that high-z galaxies are on average cooler than the $z = 0$ relation, while Sklias et al. (2014) and our results report warmer than average results for high-z galaxies. The dotted red line represents the SPIRE 250 μm detection limit as a function of dust temperature for $z = 2.9$ galaxies, illustrating the usefulness of gravitational lensing, to push to fainter objects, when studying high-z SMGs.

density measurements of Berciano Alba et al. (2010) at 1.4 GHz and the amplification factors in Table 1, the unlensed 1.4 GHz flux density for Galaxy 5 is (11 ± 1) μJy. With these two measurements, we can calculate the logarithmic ratio of the far-IR flux to radio flux density, $q_{\mathrm{IR}} = \log_{10}[(S_{\mathrm{IR}}/3.75 \times 10^{12}\,\mathrm{W\,m^{-2}})/(S_{1.4}/\mathrm{W\,m^{-2}\,Hz^{-1}})]$. We assume a power law for the radio SED, $S_{\mathrm{radio}} \propto \nu^{\alpha}$, with $\alpha = -0.8$, and we K-correct for redshift. We find $q_{\mathrm{IR}} = 1.67 \pm 0.09$, which is 2σ below the relation found by Ivison et al. (2010b) for high-z galaxies, $q_{\mathrm{IR}} = 2.3 \pm 0.3$. This indicates that Galaxy 5 may have excess radio emission, suggesting contribution from an AGN, rather than radio emission associated with star formation. For this reason, we tend to follow the results which come from our model fitting, i.e. that Galaxy 6 dominates the far-IR emission. Nevertheless, it remains the case that interpretation of this pair is difficult with existing data.

Using Atacama Large Millimeter Array (ALMA) to obtain high-resolution imaging, Hodge et al. (2013) recently showed that many of the SMGs previously detected in the LABOCA ECDFS Submillimeter Survey (LESS) are in fact composed of multiple fainter sources. The group of galaxies behind MS 0451.6−0305, consisting of Galaxies 2 through 8, is another good example of SMGs being composed of several sources. Unlensed, this $z \sim 2.9$ group would appear as a point source to any of the current single-dish submm telescopes, with flux densities of 3.8 ± 0.5, 8.5 ± 0.9, 10.4 ± 1.1, 8.0 ± 0.9, 8.9 ± 1.0, and 2.5 ± 0.3 mJy at 160, 250, 350, 500, 450, and 850 μm, respectively. This would put the group below the LESS survey detection threshold of 4.5 mJy at 870 μm; hence, we are seeing evidence of submm source multiplicity due to physically associated groupings, as opposed to chance alignment, extending to

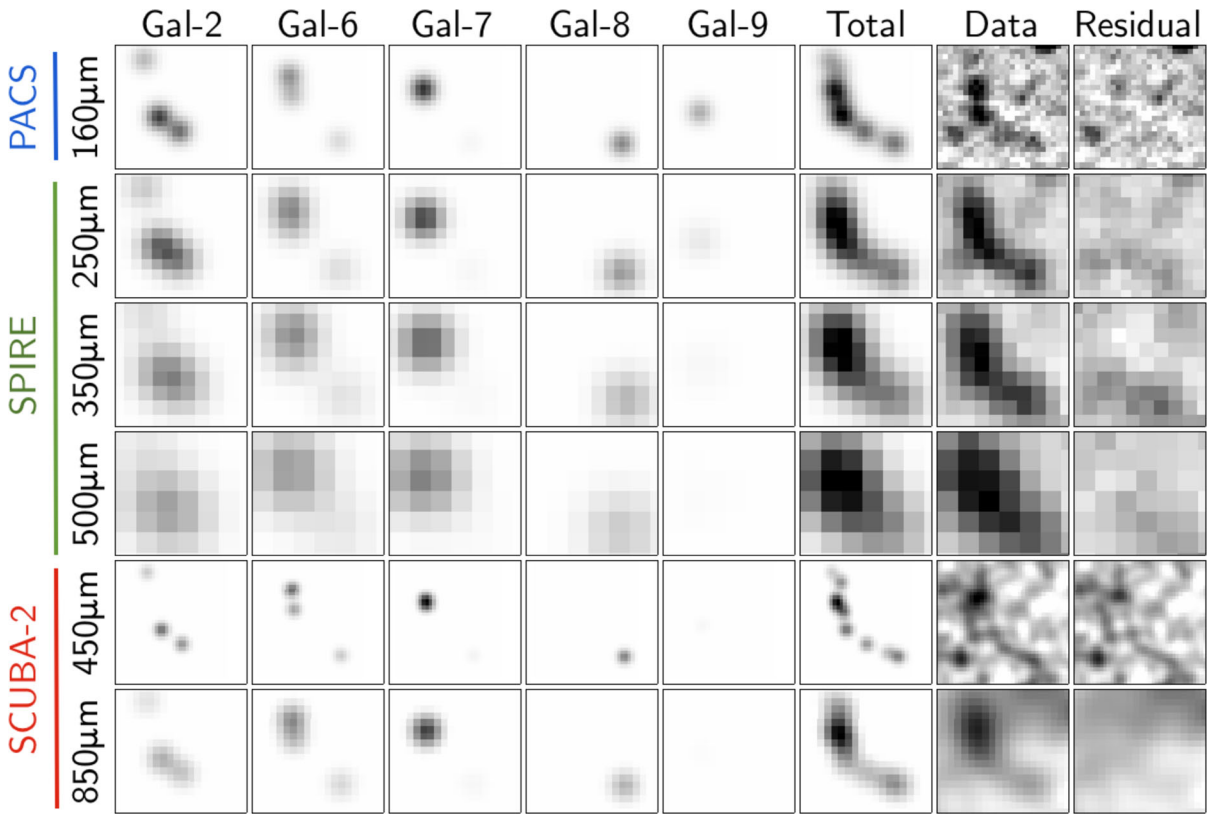

Figure 5. Decomposition of the submm arc into each contributing galaxy for the best-fitting model, the total emission for the best-fitting model, the data, and the residual after subtracting the model from the data. The columns display the contributions for individual galaxies across the six wavelength channels. Due to the differential amplification and unique positions of the multiple images, the emission from each galaxy is morphologically unique and this is what enables us to disentangle their contributions. The data and residual components for the SCUBA-2 channels have been smoothed with the FWHM for each respective wavelength. The pixel sizes are 3, 6, 8.3, 12, 2, and 4 arcsec at 160, 250, 350, 500, 450, and 850 μm, respectively.

fainter flux densities. On account of the frequency of submm source multiplicity, Hodge et al. (2013) suggest that many are likely to be physically associated. Our findings support this claim and suggest that these systems could be part of larger groups, many of which are too faint to be detected in the submm at current depths. The coincidence of being highly magnified by a massive foreground cluster allows us to study this group in much greater detail than would otherwise be possible, but we cannot infer how rare such SMG groups might be.

Although not as striking, a few analogues of our lensed star-forming galaxy group are found in the literature. First of all SMM J09431+4700, a SCUBA-selected hyperluminous IR galaxy behind A851 at $z = 3.35$ (Cowie, Barger & Kneib 2002; Ledlow et al. 2002). It is accompanied by an optically selected galaxy, DG 433 (Trager et al. 1997), separated by 400 km s^{-1} in redshift and 1 Mpc in projection. Secondly, there is SMM J16359+6612, a faint SCUBA-selected galaxy behind A2218 at $z = 2.5165$ (Kneib et al. 2004; Sheth et al. 2004). It is accompanied by two optically selected galaxies, separated by only 100 km s^{-1} in redshift and 130 kpc in projection. With more unlensed analogues of groups and recent mergers in the literature (e.g. Frayer et al. 1998; Ivison et al. 1998, 2010a, 2013; Borne et al. 2000; Tacconi et al. 2008) and the ALMA multiplicity results from Hodge et al. (2013), it is clear that mergers and interactions play an important role for many SMGs. These distant galaxy groups are akin to nearby compact groups (Hickson 1982), with the $z \sim 2.9$ galaxy group presented here reminiscent perhaps to Stephan's Quintet (Stephan 1877), due to the remarkable number of galaxies associated with this submm source. There are surely more such systems to be discovered.

However, we believe that situations like we found here are fairly rare, and it is possible that what we have described in this paper is the largest compact group that is lensed by a rich galaxy cluster on the entire sky. Although a detailed estimate of the probability is clouded by the usual problems with a posteriori statistics (i.e. if we only consider systems exactly like we found, then the probability would be arbitrarily small), we can carry out a crude estimate as follows. The MS0451 cluster has a mass of around 10^{15} M$_\odot$ (Donahue et al. 2003) and an Einstein radius of around 30 arcsec. Conservatively taking 3×10^{14} M$_\odot$ as the limit for rich clusters, surveys (like the Planck catalogue of Sunyaev–Zeldovich sources; Planck Collaboration XXIX 2013) suggest that there are around 2000 such clusters on the sky, and hence the sum of the areas covered by their Einstein radii (where strong lensing is possible) is about 10^{-5} of the sky. Assuming that a compact group has a mass of at least 3×10^{13} M$_\odot$, then the Press–Schechter formalism (Press & Schechter 1974) suggests a comoving density of about 10^{-6} Mpc^{-3} at $z = 3$ for such groups. Taking a volume that covers $\Delta z = 1$ centred on $z = 3$, we estimate 500 000 such groups on the sky. Finally, multiplying this by the fraction of the sky that might be strongly lensed by rich clusters, we find that there will only be a handful of high-redshift compact groups lensed by a rich cluster.

5.2 Physical properties

The SED fits within our model allow us to investigate the physical conditions of each component of the submm arc. Fig. 4 plots T_d versus L_IR for the four $z \sim 2.9$ galaxies constrained by our model with trends and data found by Symeonidis et al. (2013), Swinbank

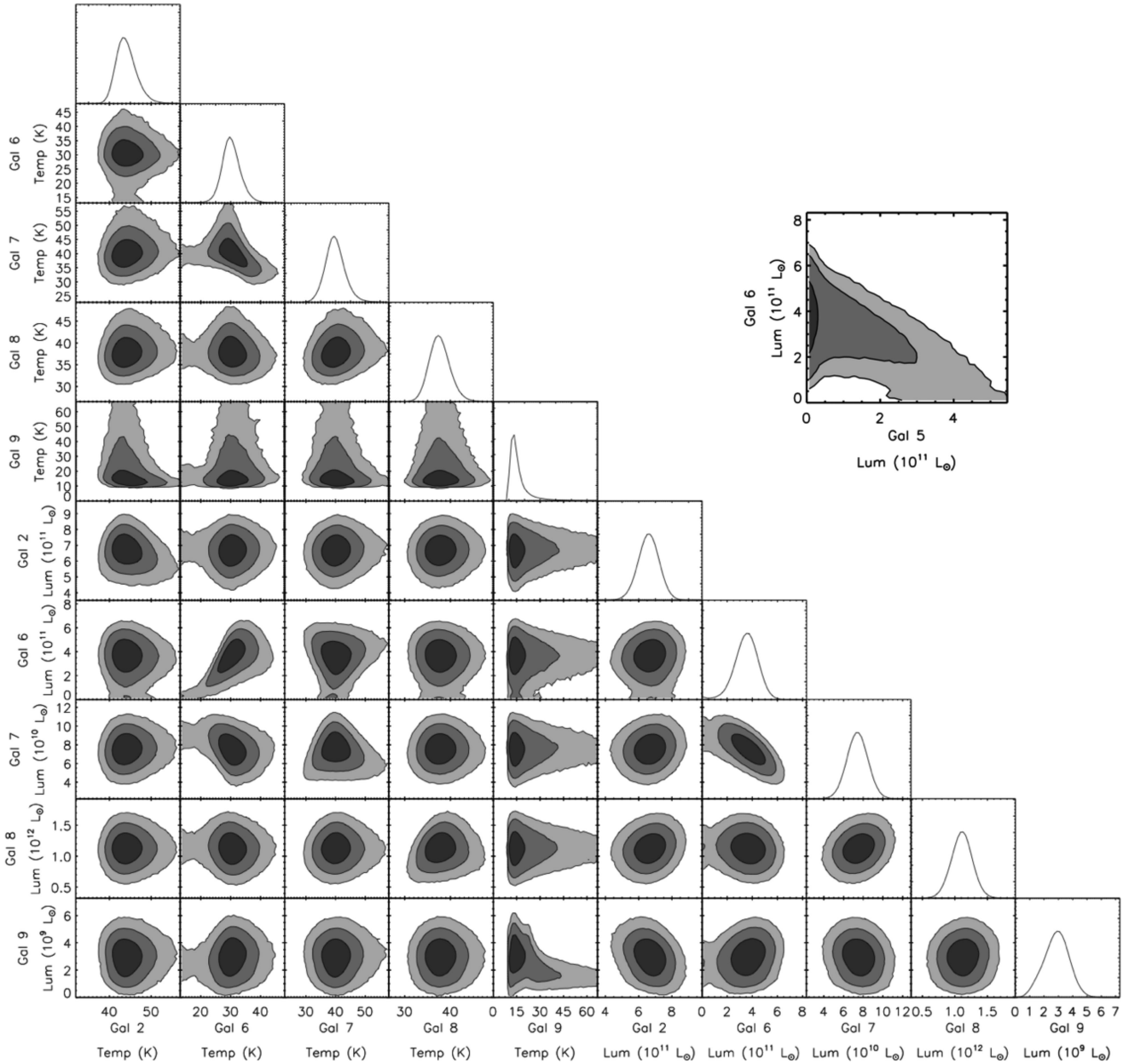

Figure 6. MCMC likelihood contours for temperature and far-IR luminosity for the galaxies that were found to contribute to the submm arc. The contour levels are 68, 95, and 99.7 per cent confidence intervals. Because of the morphological uniqueness of the lensing for each individual galaxy, there are few degeneracies here, despite the images of the system being spatially confused. The most obvious degeneracy is between the far-IR luminosity of Galaxies 6 and 7. Top-right panel: the likelihood contours for the model show a degeneracy between Galaxies 5 and 6 in far-IR luminosity. Galaxy 5 has associated radio emission, but it exceeds that expected from SFR alone, thus suggesting an AGN component.

et al. (2014), Sklias et al. (2014), and Smail et al. (2014). As described in Symeonidis et al. (2013), studying the relation between these two quantities gives insight into the nature of star formation within galaxies: a flat relation with $T_{\rm d}$ = constant implies that star formation regions become more extended when increasing far-IR luminosity, while something close to the Stefan–Boltzmann law, $L_{\rm IR} \propto T^4$, would imply constant star formation region size (for optically thick star-forming clouds). Symeonidis et al. (2013) used *Herschel* SPIRE and PACS to probe this relation and found the trend plotted as a solid black line in Fig. 4, with dashed lines showing the dispersion. When comparing low- and high-redshift galaxies, they found that the latter were up to 10 K cooler than their low-redshift counterparts, suggesting evolution with redshift towards more extended star-forming regions in the early universe. Swinbank et al. (2014) found a similar trend with high-redshift galaxies being on average 2–3 K colder than low-redshift galaxies. Smail et al. (2014) found that stacking on narrow-band [O II] emitters and MIPS+radio sources within a $z = 1.6$ cluster (intrinsically faint sources) found no evidence of evolution, although their direct detections with SPIRE and SCUBA-2 (thus intrinsically luminous sources) were also found to be cooler in temperature. A recent study by Sklias et al. (2014) used gravitational lensing to examine intrinsically fainter galaxies at high redshifts. Although limited by small number statistics, they found the opposite trend for high-redshift galaxies. When adding the

Table 2. Lensing-amplification-corrected results from the model. The total $L_{\rm FIR}$ for the $z \sim 2.9$ galaxy group is $(3.1 \pm 0.3) \times 10^{12}$ $L_\odot$, which gives an SFR of (450 ± 50) $M_\odot$ yr^{-1}. The 95th percentile upper limits are given for galaxies not found to be contributing to the submm arc. Note that Galaxy 9 is a foreground galaxy at $z = 0.157$ and is therefore not lensed.

Gal ID	$T_{\rm d}$ (K)	$L_{\rm FIR}$ ($L_\odot$)	SFR ($M_\odot$ yr^{-1})	S_{160} (mJy)	S_{250} (mJy)	S_{350} (mJy)	S_{500} (mJy)	S_{450} (mJy)	S_{850} (mJy)
1	–	$<8.2 \times 10^9$	<1.3	–	–	–	–	–	–
2	44 ± 3	$(6.7 \pm 0.6) \times 10^{11}$	99 ± 9	0.94 ± 0.10	1.9 ± 0.2	1.9 ± 0.2	1.2 ± 0.2	1.4 ± 0.2	0.31 ± 0.06
3	–	$<1.5 \times 10^{11}$	<23	–	–	–	–	–	–
4	–	$<3.3 \times 10^{11}$	<50	–	–	–	–	–	–
5	–	$<2.0 \times 10^{11}$	<35	–	–	–	–	–	–
6	31 ± 4	$(3.6 \pm 0.9) \times 10^{11}$	53 ± 14	0.31 ± 0.12	0.7 ± 0.3	1.3 ± 0.4	1.5 ± 0.4	1.5 ± 0.4	0.7 ± 0.2
7	40 ± 3	$(7.5 \pm 1.0) \times 10^{10}$	11 ± 2	0.10 ± 0.02	0.22 ± 0.04	0.23 ± 0.06	0.16 ± 0.05	0.18 ± 0.04	0.04 ± 0.02
8	37 ± 2	$(1.9 \pm 0.3) \times 10^{12}$	290 ± 40	2.5 ± 0.4	5.6 ± 0.8	6.9 ± 1.0	5.1 ± 0.9	5.8 ± 1.0	1.5 ± 0.3
9	*17 ± 9*	$(1.7 \pm 0.5) \times 10^9$	0.25 ± 0.07	3.6 ± 1.0	2.5 ± 0.8	1.3 ± 0.5	0.5 ± 0.2	0.6 ± 0.2	0.08 ± 0.04

four $z \sim 2.9$ galaxies constrained by our model, our results appear to support those found by Sklias et al. (2014). This suggests that selection effects and/or biases are present in the different studies.

As has been pointed out before (e.g. Chapman et al. 2005; Chapin et al. 2011), selection effects can be extremely important when studying the correlation between $T_{\rm d}$ and $L_{\rm IR}$. The Swinbank et al. (2014) sample of SMGs were selected at 870 μm, and thus may be biased towards lower dust temperatures, and those of Sklias et al. (2014) were formally selected at 160 μm, and thus could be biased towards warmer dust temperatures. It should be noted that the submm arc in MS 0451.6−0305 was first discovered at 850 μm (Chapman et al. 2002a), and therefore is unlikely to be biased towards the warmer dust temperatures that we find.

In addition to the selection biases inherent in focusing on a single distinctive source, there are also a number of systematic uncertainties that could be present in our modelling approach. Most importantly, we have fixed the amplification factors for the galaxy images. Any errors in amplification can affect our results in several ways. For example, since the contributions to the submm arc from Galaxies 7 and 8 (See Fig. 5) are mostly point-like, any uncertainty in amplification predominantly affects their measured far-IR luminosities and SFRs. This is especially true for Galaxy 7, because two of its images lie very close to the critical line, and thus its amplification is highly sensitive to any offset between optical and submm components of the galaxy. The uncertainty in relative amplification between galaxy images likely affects which galaxies are preferred by the data. For example, the images of Galaxies 5 and 6 are spatially very close; thus, the different relative amplifications between their respective images probably contribute to Galaxy 6 being preferred by the model fits.

It is possible that the simple SED model we have adopted may not accurately approximate the true SEDs of the galaxies in the lensed system. The dust emissivity, β, is known to be partially degenerate with dust temperature and we have fixed it to a nominal value of 1.5; thus, the uncertainties reported for dust temperatures are likely too small. Furthermore, although these newer *HST* data are both deeper and at a longer wavelength, it is possible that we are missing fainter group members, as was the case in previous studies (Borys et al. 2004; Berciano Alba et al. 2010). If any of the galaxies are not at $z \sim 2.9$, their reported far-IR luminosities and thus SFRs will be affected, since the distances to the galaxies are used in these calculations. This is especially true for Galaxy 8, as we have no constraints on its actual redshift and our analysis has assumed it to be part of the $z \sim 2.9$ group.

Despite these reservations, the model we have adopted appears to provide a reasonably good fit to the data across a wide range of wavelengths. Higher resolution submm data would be needed to further investigate the nature of the $z \sim 2.9$ galaxy group.

6 CONCLUSIONS

With our new modelling approach, we have overcome the confused nature of this complex system by fully exploiting the differential amplification across the galaxy group and the multiple imaging caused by the strong gravitational lensing. This has allowed us to tackle the challenge of disentangling and fitting SEDs to multiple components of the submm arc. We have shown that the submm arc is predominantly generated by four of the seven galaxies that probably comprise a group at a redshift of $z \sim 2.9$, with star formation likely triggered by the galaxies undergoing a merger. It is therefore not necessary to have a hidden region of dust-enshrouded star formation (as postulated by Berciano Alba et al. 2010) to explain the morphology of the submm arc. This method also demonstrates the power of a broad multiwavelength approach to fully understanding the nature of the submm arc: *HST* imaging gives us the priors on galaxy positions, as well as providing the constraints for the lensing model; *Herschel* samples the peak of the far-IR SED, as well as providing the high-resolution far-IR imaging at 160 μm; and SCUBA-2 850 μm data sample the long-wavelength portion of the FIR SED at a resolution that closely matches that of the 160 μm imaging.

This is a unique system that gives us a glimpse into the formation of structure and stars in the early Universe, and no other submm lens discovered to date can match the number of separate galaxies lensed from the same redshift. Spectroscopy and high-resolution follow-up with new interferometer observatories will be the key to confirming and unravelling the nature of this high-z merging galaxy group.

ACKNOWLEDGEMENTS

This research has been supported by the Natural Sciences and Engineering Research Council of Canada. IRS acknowledges support from STFC (ST/I001573/1), a Leverhulme Fellowship, the ERC Advanced Investigator programme DUSTYGAL, and a Royal Society/Wolfson merit award. The James Clerk Maxwell Telescope is operated by the Joint Astronomy Centre on behalf of the Science and Technology Facilities Council of the United Kingdom, the National Research Council of Canada, and (until 2013 March 31) the Netherlands Organization for Scientific Research. Additional funds for the construction of SCUBA-2 were provided

by the Canada Foundation for Innovation. SPIRE has been developed by a consortium of institutes led by Cardiff University (UK) and including University of Lethbridge (Canada); NAOC (China); CEA, LAM (France); IFSI, University of Padua (Italy); IAC (Spain); Stockholm Observatory (Sweden); Imperial College London, RAL, UCL-MSSL, UKATC, University of Sussex (UK); and Caltech, JPL, NHSC, University of Colorado (USA). This development has been supported by national funding agencies: CSA (Canada); NAOC (China); CEA, CNES, CNRS (France); ASI (Italy); MCINN (Spain); SNSB (Sweden); STFC, UKSA (UK); and NASA (USA). PACS has been developed by a consortium of institutes led by MPE (Germany) and including UVIE (Austria); KU Leuven, CSL, IMEC (Belgium); CEA, LAM (France); MPIA (Germany); INAF-IFSI/OAA/OAP/OAT, LENS, SISSA (Italy); IAC (Spain). This development has been supported by the funding agencies BMVIT (Austria), ESA-PRODEX (Belgium), CEA/CNES (France), DLR (Germany), ASI/INAF (Italy), and CICYT/MCYT (Spain). This research has made use of data from the HerMES project (http://hermes.sussex.ac.uk/), a Herschel Key Programme utilizing Guaranteed Time from the SPIRE instrument team, ESAC scientists, and a mission scientist. The HerMES data were accessed through the HeDaM data base (http://hedam.oamp.fr) operated by CeSAM and hosted by the Laboratoire d'Astrophysique de Marseille. This research used the facilities of the Canadian Astronomy Data Centre operated by the National Research Council of Canada with the support of the Canadian Space Agency. This work is based on observations made with the NASA/ESA *Hubble Space Telescope*, obtained from the data archive at the Space Telescope Institute. STScI is operated by the association of Universities for Research in Astronomy, Inc. under the NASA contract NAS 5-26555. This work is also based (in part) on observations made with the *Spitzer Space Telescope*, which is operated by the Jet Propulsion Laboratory, California Institute of Technology under a contract with NASA. Support for this work was provided by NASA. The Dark Cosmology Centre is funded by the Danish National Research Council.

REFERENCES

Amblard A. et al., 2010, A&A, 518, L9
Bendo G. J. et al., 2013, MNRAS, 433, 3062
Berciano Alba A., Koopmans L. V. E., Garrett M. A., Wucknitz O., Limousin M., 2010, A&A, 509, A54
Borne K. D., Bushouse H., Lucas R. A., Colina L., 2000, ApJ, 529, L77
Borys C. et al., 2004, MNRAS, 352, 759
Casey C. M., 2012, MNRAS, 425, 3094
Chapin E. L. et al., 2011, MNRAS, 411, 505
Chapin E. L., Berry D. S., Gibb A. G., Jenness T., Scott D., Tilanus R. P. J., Economou F., Holland W. S., 2013, MNRAS, 430, 2545
Chapman S. C., Scott D., Borys C., Fahlman G. G., 2002a, MNRAS, 330, 92
Chapman S. C., Smail I., Ivison R. J., Helou G., Dale D. A., Lagache G., 2002b, ApJ, 573, 66
Chapman S. C., Blain A. W., Smail I., Ivison R. J., 2005, ApJ, 622, 772
Colley W. N., Tyson J. A., Turner E. L., 1996, ApJ, 461, L83
Cowie L. L., Barger A. J., Kneib J.-P., 2002, AJ, 123, 2197
Dale D. A. et al., 2012, ApJ, 745, 95
Dempsey J. T. et al., 2013, MNRAS, 430, 2534
Donahue M., Gaskin J. A., Patel S. K., Joy M., Clowe D., Hughes J. P., 2003, ApJ, 598, 190
Frayer D. T., Ivison R. J., Scoville N. Z., Yun M., Evans A. S., Smail I., Blain A. W., Kneib J.-P., 1998, ApJ, 506, L7
Fu H. et al., 2012, ApJ, 753, 134
Geach J. et al., 2006, ApJ, 649, 661
Geman S., Geman D., 1993, J. Appl. Stat., 20, 25
Gioia I. M., Luppino G. A., 1994, ApJS, 94, 583
Griffin M. J. et al., 2010, A&A, 518, L3
Hastings W. K., 1970, Biometrika, 57, 97
Hickson P., 1982, ApJ, 255, 382
Hodge J. A. et al., 2013, ApJ, 768, 91
Holland W. S. et al., 2013, MNRAS, 430, 2513
Ivison R. J., Smail I., Le Borgne J.-F., Blain A. W., Kneib J.-P., Bezecourt J., Kerr T. H., Davies J. K., 1998, MNRAS, 298, 583
Ivison R. J., Smail I., Papadopoulos P. P., Wold I., Richard J., Swinbank A. M., Kneib J.-P., Owen F. N., 2010a, MNRAS, 404, 198
Ivison R. J. et al., 2010b, A&A, 518, L31
Ivison R. J. et al., 2013, ApJ, 772, 137
Jullo E., Kneib J.-P., 2009, MNRAS, 395, 1319
Jullo E., Kneib J.-P., Limousin M., Elíasdóttir Á., Marshall P. J., Verdugo T., 2007, New J. Phys., 9, 447
Karim A. et al., 2013, MNRAS, 432, 2
Kennicutt R. C., Jr, 1998, ARA&A, 36, 189
Kneib J.-P., Ellis R. S., Smail I., Couch W. J., Sharples R. M., 1996, ApJ, 471, 643
Kneib J.-P., van der Werf P. P., Kraiberg Knudsen K., Smail I., Blain A., Frayer D., Barnard V., Ivison R., 2004, MNRAS, 349, 1211
Kochanek C. S., Narayan R., 1992, ApJ, 401, 461
Kodama T. et al., 2005, PASJ, 57, 309
Kovács A., Chapman S. C., Dowell C. D., Blain A. W., Ivison R. J., Smail I., Phillips T. G., 2006, ApJ, 650, 592
Ledlow M. J., Smail I., Owen F. N., Keel W. C., Ivison R. J., Morrison G. E., 2002, ApJ, 577, L79
Lehnert M. D., Heckman T. M., 1996, ApJ, 472, 546
Levenson L. et al., 2010, MNRAS, 409, 83
Lewis A., Bridle S., 2002, Phys. Rev. D, 66, 103511
Lutz D. et al., 2011, A&A, 532, A90
Metropolis N., Rosenbluth A. W., Rosenbluth M. N., Teller A. H., Teller E., 1953, J. Chem. Phys., 21, 1087
Meurer G. R., Heckman T. M., Lehnert M. D., Leitherer C., Lowenthal J., 1997, AJ, 114, 54
Moran S. M., Ellis R. S., Treu T., Smith G. P., Rich R. M., Smail I., 2007, ApJ, 671, 1503
Muller T., Nielbock M., Balog Z., Klass U., Vilenius E., 2011, Technical Report PICC-ME-TN-037, available at: http://herschel.esac.esa.int/twiki/pub/Public/PacsCalibrationWeb/pacs_bolo_fluxcal_report_v1.pdf
Murphy E. J. et al., 2011, ApJ, 737, 67
Negrello M. et al., 2010, Science, 330, 800
Nguyen H. T. et al., 2010, A&A, 518, L5
Oliver S. J. et al., 2012, MNRAS, 424, 1614
Ott S., 2010, in Mizumoto Y., Morita K.-I., Ohishi M., eds, ASP Conf. Ser. Vol. 434, Astronomical Data Analysis Software and Systems XIX. Astron. Soc. Pac., San Francisco, p. 139
Pascale E. et al., 2009, ApJ, 707, 1740
Pilbratt G. L. et al., 2010, A&A, 518, L1
Planck Collaboration XXIX, 2013, preprint (arXiv:1303.5089P)
Poglitsch A. et al., 2010, A&A, 518, L2
Pope A. et al., 2006, MNRAS, 370, 1185
Press W. H., Schechter P., 1974, ApJ, 187, 425
Reese E. D. et al., 2000, ApJ, 533, 38
Serjeant S., 2012, MNRAS, 424, 2429
Sheth K., Blain A. W., Kneib J.-P., Frayer D. T., van der Werf P. P., Knudsen K. K., 2004, ApJ, 614, L5
Sklias P. et al., 2014, A&A, 561A, 149S
Smail I., Ivison R. J., Blain A. W., 1997, ApJ, 490, L5
Smail I. et al., 2014, ApJ, 782, 19
Stephan M., 1877, MNRAS, 37, 334
Swinbank A. M. et al., 2014, MNRAS, 438, 1267S
Swinyard B. M. et al., 2010, A&A, 518, L4
Symeonidis M. et al., 2013, MNRAS, 431, 2317
Tacconi L. J. et al., 2008, ApJ, 680, 246
Takata T. et al., 2003, PASJ, 55, 789
Trager S. C., Faber S. M., Dressler A., Oemler A., Jr, 1997, ApJ, 485, 92

Viero M. P. et al., 2013, ApJ, 772, 77
Wardlow J. L. et al., 2010, MNRAS, 401, 2299
Wardlow J. L. et al., 2013, ApJ, 762, 59
Zitrin A., Broadhurst T., Barkana R., Rephaeli Y., Benítez N., 2011, MNRAS, 410, 1939

[1]*Department of Physics & Astronomy, University of British Columbia, 6224 Agricultural Road, Vancouver, BC V6T 1Z1, Canada*
[2]*Institute for Computational Cosmology, Department of Physics, Durham University, South Road, Durham DH1 3LE, UK*
[3]*XMM–Newton SOC, European Space Astronomy Centre, ESA, E-28691 Villanueva de la Cañada, Spain*
[4]*Department of Physics and Atmospheric Science, Dalhousie University, 6310 Coburg Rd., Halifax, NS B3H 4R2, Canada*
[5]*Center for Astrophysics and Space Astronomy 389-UCB, University of Colorado, Boulder, CO 80309, USA*
[6]*Department of Physics & Astronomy, University of California, Irvine, CA 92697, USA*
[7]*California Institute of Technology, 1200 E. California Blvd., Pasadena, CA 91125, USA*
[8]*Institute for Astronomy, University of Edinburgh, Royal Observatory, Blackford Hill, Edinburgh EH9 3HJ, UK*
[9]*Department of Physics, Virginia Tech, VA 24061, USA*
[10]*Department of Physics and Astronomy, University of Waterloo, Waterloo, ON N2L 3G1, Canada*
[11]*UK Astronomy Technology Centre, Royal Observatory, Edinburgh, Blackford Hill, Edinburgh EH9 3HJ, UK*
[12]*Joint Astronomy Centre, 660 N. A'ohōkū Place, University Park, Hilo, HI 96720, USA*
[13]*Department of Astronomy, Cornell University, Ithaca, NY 14853, USA*
[14]*Laboratoire dastrophysique, Ecole Polytechnique Fédérale de Lausanne, Observatoire de Sauverny, CH-1290 Versoix, Switzerland*
[15]*CRAL, Observatoire de Lyon, Université Lyon 1, 9 Avenue Ch. André, F-69561 Saint Genis Laval Cedex, France*
[16]*Herschel Science Centre, European Space Astronomy Centre, ESA, E-28691 Villanueva de la Cañada, Spain*
[17]*Dark Cosmology Centre, Niels Bohr Institute, University of Copenhagen, Juliane Maries Vej 30, DK-2100 Copenhagen, Denmark*

This paper has been typeset from a TEX/LATEX file prepared by the author.